Synthesis of zero-valent iron/biochar by carbothermal reduction from wood waste and iron mud for removing rhodamine B

Chao Chen (cchao1990@163.com)
Tsinghua University https://orcid.org/0000-0001-9127-9630
Jianguo Liu
Tsinghua University
Chao Gen
Tsinghua University
Qin Liu
Tsinghua University
Xuetao Zhu
Tsinghua University
Wenzhi Qi
Tsinghua University
Fan Wang
Tsinghua University

Research Article

Keywords: Wood waste, Iron mud, Carbothermal reduction, zero-valent iron/biochar, Rhodamine B

Posted Date: March 16th, 2021

DOI: https://doi.org/10.21203/rs.3.rs-158094/v1

Synthesis of zero-valent iron/biochar by carbothermal reduction from wood waste and iron mud for removing rhodamine B

Chao Chen, Jianguo Liu*, Chao Gen, Qin Liu, Xuetao Zhu, Wenzhi Qi, Fan Wang

School of Environment, Tsinghua University, Beijing 100084, China

✉ jgliu@tsinghua.edu.cn

GRAPHICAL ABSTRACT

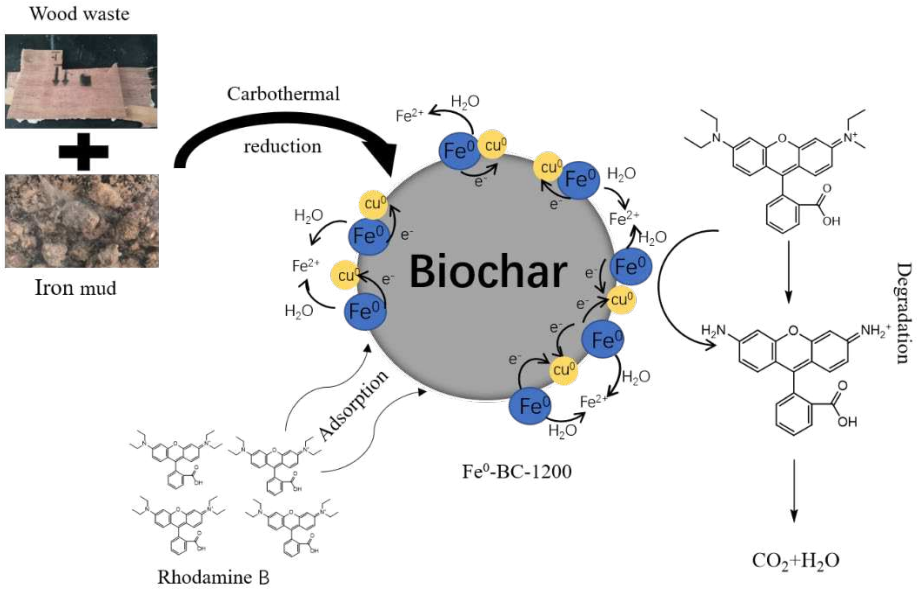

ABSTRACT

This study proposes a new process to synthesize zero-valent iron/biochar (Fe^0-BC) by carbothermal reduction using wood waste and iron mud as raw materials under different temperature. The characterization results showed that the Fe^0-BC synthesized at 1200ºC (Fe^0-BC-1200) possessed favorable adsorption capacity with the specific surface area of 103.18 m^2/g, and that the zero-valent iron (Fe^0) particles were uniformly dispersed on the biochar surface. The removal efficiency of rhodamine B (RB) was determined to evaluate the performance of the prepared Fe^0-BC. Fe^0-BC-1200 presented the best performance on RB removal, which mainly ascribe to that more Fe^0 particles generated at higher temperature. The equilibrium adsorption capacity reached 49.93 mg/g when the initial RB concentration and the Fe^0-BC-1200 dosage were 100 mg/L and 2g/L, respectively, and the pseudo-second-order model was suitable to fit the removal experimental data. LCMC and XRD analyses revealed that the removal mechanism included the physical adsorption of biochar and the redox reaction of Fe^0. Moreover, copper existed in the iron mud was also reduced to Cu^0, which was beneficial to catalyze the oxidation of iron, the degradation of RB was promoted at the same time.

Keywords: Wood waste; Iron mud; Carbothermal reduction; zero-valent iron/biochar; Rhodamine B.

Introdution

In recent years, with the rapid growth in the living standard in China, the life cycle of many furniture is becoming shorter and shorter, and frequent housing rental activities increase the probability of wood waste being abandoned. According to statistics, about 85 million m^3 of bulky wood waste are produced every year in China. The main component of wood waste is wood, and the carbon content is between 40% and 50% (Emandi et al., 2011; Tsoumis, 2013; Demirbaş, 2005). Thus, preparing biochar by pyrolysis of wood waste is one of the effective recycling methods. Biochar shows outstanding potential for removing organic contaminants from the environment by possessing abundant oxygen-containing functional groups and large surface area (Liu et al., 2015; Zhang et al., 2019; Huang et al., 2018; Wang et al., 2018). However, the application of biochar in wastewater has some problems, such as difficult separation and incomplete removal (Chen et al., 2011; Du et al., 2020). To overcome these shortcomings, many researchers loaded zero-valent iron (Fe^0) on biochar surface to synthesize zero-valent iron/biochar (Fe^0-BC). Fe^0, especially nano size Fe^0 is also an excellent environmental remediation material has been widely used in wastewater and contaminated soil treatment due to its high reducibility for heavy metals and organic matter (Pourrezaei et al., 2014; Reddy et al.,2016; Calderon and Fullana 2015; Ghariani et al., 2019). As a combination, Fe^0-BC has the advantages of both biochar and Fe^0, thereby it provides higher reduction or degradation efficiency and other benefits including easiness to recycle, non- aggregation. (Bakshi et al., 2018; Li et al.,2020; Dong et al., 2017; Li et al., 2019;). More and more studies proved that Fe^0-BC show better performance in removing different contaminants through reduction, adsorption, precipitation and other mechanisms (Frick et al.,2016; Oh et al., 2016; Oleszczuk and Kołtowski 2017; Mitzia et al.,2020).

In order to obtained the more valuable Fe^0-BC, the other solid waste, iron mud could be used as an iron resource for collaborative utilization with wood waste. Iron mud refers to the waste slag with high iron content produced in chemical industrial production, such as dyeing and printing enterprises (Pani et al., 2019; Liu et al., 2018). The iron mud mainly contains iron oxide and organic compounds that can be recovered (Zhu et al., 2018). At present, iron mud is usually disposed by stacking, landfilling, or sending to steel plants as a raw material of iron-making in China (Liu et al., 2014). The stacking and landfilling of iron mud take up massive land, and the existing hazardous substances permeate into the underground, causing secondary pollution to the environment. For sending to steel plant, iron mud can easily block the furnace because of its fine particle size, thereby seriously reducing the product quality and complicating the recycling process.

At present, the most used widely synthesis method is the two-step method (Devi et al., 2014; Liu et al., 2015; Zhao et al., 2020; Han et al., 2019; Sun et al., 2019; Dewage et al., 2018), which refer to that the biomass is pyrolyzed to obtain biochar firstly, then strongly impregnated in the high valent iron salts, and then reduced through liquid-

phase or gas-phase reductant. Devi et al. (2014) synthesized Fe^0/BC composites from the paper mill sludge through the following process: paper mill sludge was pyrolyzed to biochar at 700 ℃, mixed with $FeSO_4 \cdot H_2O$, and then added $NaBH_4$ as a reducing agent for the reduction of Fe^{2+} to Fe^0 at the same time. Liu et al. (2015) obtained Fe^0/BC by the reduction of natural limonite and pine biomass using H_2 at 550°C. The above synthesis process needs a large number of reducing reagents, with high raw material cost and complex operation, thus, it can only be applied to laboratory research. Carbothermal reduction is another synthesis method (Lawrinenko et al., 2017; Mandal et al., 2017; Hussain et al., 2017), in which iron compounds and biomass are mixed to pyrolysis at a high temperature, the iron compounds are reduced by the reducing substances generated during biomass pyrolysis, and then Fe^0/BC is prepared by one step. Lawrinenko et al. (2017) successfully prepared Fe^0/BC through the slow pyrolysis of lignin and magnetite mixtures in a muffle furnace and heated at 900 °C for 4 h. By contrast, carbothermal reduction has the advantages of low raw material cost, simple process, easy scaling, continuous production (Shang et al., 207).

Rhodamine B (RB), $C_{28}H_{31}N_2O_3Cl$, a highly water-soluble and bright red fluorescent xanthene dye, is widely used as colorant for textiles and food industry (Long et al., 2014). However, it has been proven that RB has toxic effects on animals and humans, including carcinogenicity, reproductive toxicity and neurotoxicity (Dong et al., 2010). RB is a ubiquitous organic pollutant in printing and dyeing wastewater due to the wide application in the textile industry (Lops et al., 2019; Huang et al., 2017). Therefore, it has great significance to find a suitable process or material to remove the RB in wastewater.

The massive production and stacking of wood waste and iron mud engenders a serious environmental pollution and waste of resources. To overcome these problems, in this study, a novel process, wood waste and iron mud were used as raw materials, to synthetize Fe^0-BC through carbothermal reduction, was proposed. At the same time, the removal efficiency of RB was conducted to evaluate the performance of synthetic Fe^0-BC. The structural composition and micromorphology of synthetic Fe^0-BC was investigated. Moreover, the interaction process between the Fe^0-BC and RB was also studied.

Materials and Methods

Materials

The iron mud used in this study was obtained from a printing and dyeing factory in Shanghai, China. The chemical compositions of iron mud measured by X-ray fluorescence spectrometry (XRF) is shown in Table 1, and the X-ray diffraction (XRD) pattern of the iron mud is presented in Figure 1. The results show that the iron mud contain 41.71% Fe_2O_3, 15.23% CuO, and 10.12% C, and the main phases are magnetite (Fe_3O_4), Tenorite (CuO), organic iron ($Fe_2C_6H_{10}O_4$) and calcium aluminosilicate. Wood

waste used in this study was abandoned wooden chair from the laboratory. The chair is made of pine wood board and is not painted. The carbon content of the chair is 43.14%, which was measured by Elemental Analyzer (FlashSmart, Thermo, American).

All chemical reagents are analytically pure, and ultrapure water was used throughout this study.

Table1 Chemical compositions of the iron mud

Component	Fe_2O_3	CuO	C	CaO	Al_2O_3	SiO_2	MgO	TiO_2	P_2O_5	Na_2O
Content(%,ω)	41.71	15.23	10.12	5.24	4.43	4.31	1.37	0.65	0.12	0.08

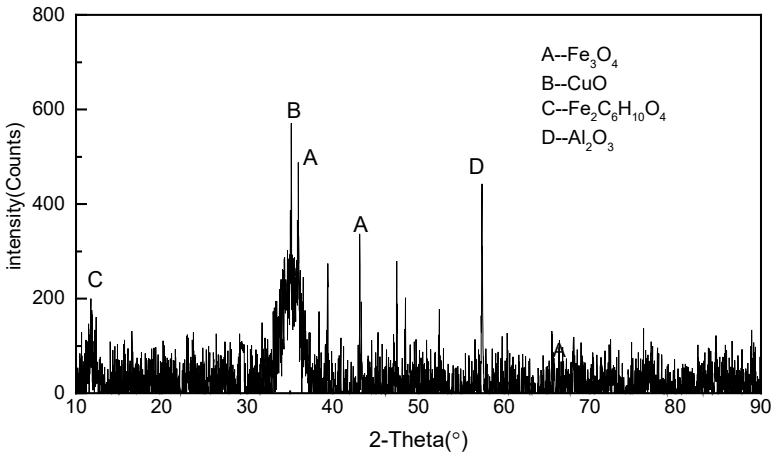

Figure 1. XRD patterns of the iron mud

Synthesis of Fe^0-BC

According to our previous related works (Geng et al.,2020; Chen et al.,2019), Fe^0-BC was prepared as shown in Figure 2. Firstly, the wooden chair and iron mud were dried in an oven for 2 h at 110 ℃ after cleaning, and then the wood flour was prepared by crushing in a crusher and passing through a 40-mesh sieve. Additionally, the wood flour and dried iron mud with a mass ratio of 1:2 were homogeneously mixed using a 150r/min roller mill for 5min, and then a 40g mixture was placed into a corundum crucible. Subsequently. carbothermal reduction of the mixture was conducted by heating under nitrogen in a sealed furnace at 800 ℃, 900 ℃, 1000 ℃,1100 ℃,1200 ℃, respectively. The furnace temperature was increased at an average of 15 ℃/min, and a 180 min holding time was applied when the temperature reached the target temperature. After roasting, the reduced product was taken out when self-cooled down to laboratory temperature. Finally, Fe^0-BC was prepared by grinding in a 200r/min rod mill for 10min and passing through a 200-mesh sieve, named as Fe^0-BC-T, where T indicates the carbothermal reduction temperature. The synthesis process was repeated three times at each temperature. The subsequent experimental data used for plotting graphs is the average value of three experimental data.

After synthesis of Fe^0-BC-T, some samples were cleaned repeatedly using 2mol/L HCl until no change in weight after drying. And then the biochar without Fe was obtained, named as BC-T.

Figure 2. The preparation process of Fe^0-BC

Characterizations

The pore-structure parameters were measured by specific surface area and porosity analyzer (ASAP2010, Micromeritics, American) using N_2 adsorption method. The phase composition present in the samples was detected by XRD (D/max-2550, Rigaku, Japan) with Cu K_α radiation over a 2θ collection range of 10°~90°. Micromorphology was analyzed by scanning electron microscope (SEM), and energy dispersive spectrometry (EDS) ((JSM-6460LV, JEOL, Japan).

Removal experiments

The removal efficiency of RB on different materials was investigated, including the Fe^0-BC-T, BC-T and the purchased Fe^0 powder. 1.6 g of each material (2g/L) was added into a 1000 mL conical flask with 800 mL RB solution with an initial concentration of 100 mg/L and an initial pH ranging from 1.5 to 6. The pH of the prepared 100mol/L RB solution is 4.02. The target initial pH value of solution was adjusted by diluted HCl or NaOH. The conical flasks were placed in a 60 r/min shaker at 25 °C, and 5ml of suspension extracted from flask was filtered with a 0.45 μm microporous filtration membrane at predetermined time intervals. Meanwhile, the solution pH value was recorded during the whole removal process. The residual RB concentrations were evaluated by ultraviolet and visible spectrophotometry (UV-Vis) (5B-3B, Lian-hua, China). RB removal capacity and removal efficiency can be obtained by Eq. (1) and Eq. (2), respectively.

$$q_e = \frac{C_0 - C_e}{m} V \quad (1)$$

$$R = \frac{C_0 - C_t}{C_0} \times 100 \quad (2)$$

Where q_e, R, m, V stand for the RB removal capacity (mg/g), removal efficiency (%), RB solution volume (L), and the dose (g) of materials. C_0, C_e, C_t stand for initial concentration (mg/L), equilibrium concentration (mg/L) and residual concentration (mg/L) at time t (min).

Adsorption kinetic of removal process was evaluated by pseudo-first order and pseudo-second-order models, as shown in Eq. (5) and Eq. (6) respectively.

$$\ln(q_e - q_t) = \ln q_e - k_1 t \quad (3)$$

$$\frac{t}{q_t} = \frac{1}{k_2 {q_e}^2} + \frac{t}{q_e} \quad (4)$$

where k_1(min^{-1}) and k_2(g/(mg·min)) stand for the sorption rate constants of quasi-first order and quasi-second order, respectively; q_e (mg/g) represent the removal capacities at the equilibrium; q_t(mg/g) represent the removal capacities at the time t (min).

Reaction products at different times were measured by LCMS (1290II-6460, Agilent, American) under the following conditions: chromatographic column of XDB-C8 4.6*150mm, 5μm, column temperature of 50℃, mobile phase of methanol-water (70:30), test time of 30min, and flow rate of 0.8mL/min.

Results and discussion

Characterization of Fe^0-BC

The XRD analysis results of Fe^0-BC prepared at different temperature are shown in Figure 3. The main phases of Fe^0-BC-800 and Fe^0-BC-900 are both Fe_3O_4 and CuO. This finding indicated that the organic iron in the mixture were pyrolyzed to Fe_3O_4, whereas the iron oxide was not reduced under 900 ℃. The diffraction peaks of CuO disappeared and the diffraction peaks of zero valent copper (Cu^0) were observed in the XRD pattern of Fe^0-BC-1000, which confirmed that CuO was reduced by the reducibility of pyrolysis products such as C, CO, H_2, as shown in Eq. (3). When the reduced temperature reached 1100 ℃, the diffraction peaks of zero valent iron (Fe^0) appeared and the diffraction peaks of Fe_3O_4 weakened, proving that part of Fe_3O_4 was reduced via Eq. (4) at this temperature (Chen et al., 2017). The main phases of Fe^0-BC-1200 are Fe^0 and Cu^0, and the iron oxide in the mixture competely reduced to Fe^0 at 1200 ℃.

$$CuO+C/CO/H_2 \longrightarrow Cu+CO/CO_2/H_2O \quad (5)$$

$$Fe_3O_4+4C/CO/H_2 \longrightarrow 3Fe+4CO/CO_2/H_2O \quad (6)$$

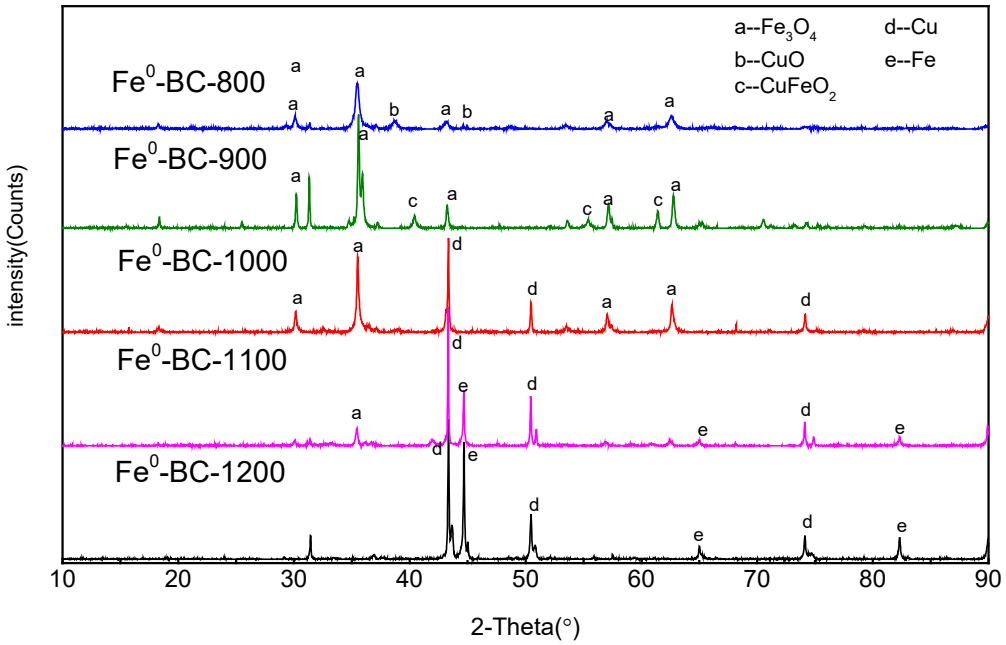

Figure 3. XRD patterns of Fe^0-BC

Table 2 shows the main element composition of different Fe^0-BC materials. As shown in Table 2, the content of C was higher than those of Fe and Cu, and the content of Fe and Cu increased with the increase of temperature. This result can be ascribed to the fact that the increase of temperature is conducive to the reduction of iron and copper compounds. Thus, the carbon reductant was consumed at a high temperature. The surface area and pore size of Fe^0-BC are shown in Table 3. It can be seen that the Fe^0-BC have similar properties in pore structure with the specific surface area is about 100 m^2/g and a pore size between 3 and 4 nm, indicating favorable adsorption performance to some extent.

Table 2 Main element contents of Fe^0-BC

Element	Fe	C	Cu
Fe^0-BC-800	23.8	44.2	16.6
Fe^0-BC-900	23.6	43.3	16.9
Fe^0-BC-1000	26.7	40.7	17.8
Fe^0-BC-1100	27.2	37.4	17.6
Fe^0-BC-1200	31.2	34.3	20.4

Table 3 The pore-structure parameters of Fe-C

Sample	specific surface area (m^2/g)	pore Diameter (nm)
Fe^0-BC-800	151.8	4.19
Fe^0-BC-900	143.6	3.32
Fe^0-BC-1000	116.7	3.35
Fe^0-BC-1100	97.2	4.21
Fe^0-BC-1200	103.18	3.69

Consistent with previous studies (Kong et al., 2018; Geng et al., 2019; Shen et al.,

2019), the above results proved that the temperature of carbothermal reduction considerably influenced the phase of Fe, and only Fe^0-BC-1200 existed no other iron-containing phases aside from Fe^0. SEM and EDS analyses were performed on Fe^0-BC-1200, and the results are shown in Figure 4. As shown in Figure 4(a), the gray part of the picture was detected as biochar and the brighter dots were detected as Fe^0. In addition, the Fe^0 particles were appropriately dispersed on the granular biochar surface. Moreover, no aggregation of iron occurred, the size Fe^0 particles of was Fe^0 particle very small, basically approached nanometer level. A random section of biochar surface was selected for EDS analysis, and the result is presented in Figure 4(b). It illustrates that the Cu^0 migrated to the biochar surface at the same time. In general, according to the previous study, the presence of Cu can form bimetals with Fe^0, that is favor to accelerate the degradation of organic pollutants by catalyzing the corrosion of iron.

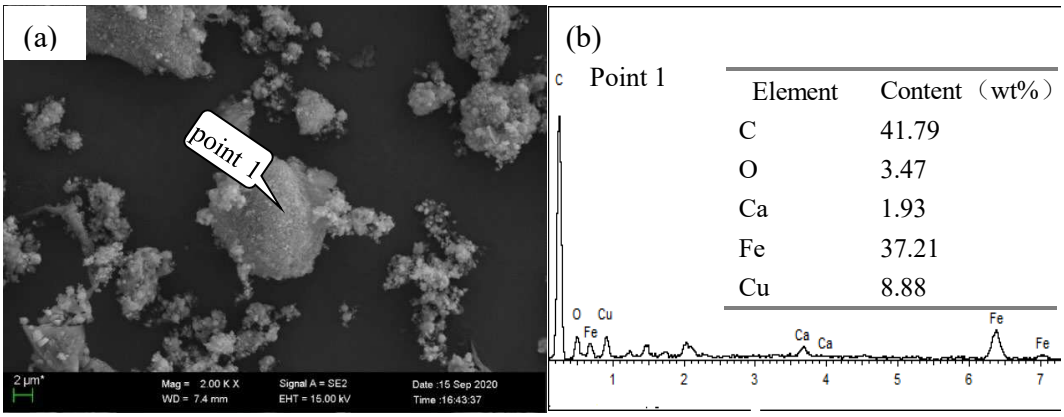

Figure 4. SEM image and EDS results of Fe^0-BC-1200

Removal performance

Removal efficiency

Figure 5 shows the removal efficiency of RB on Fe^0-BC prepared at different temperatures. It is obvious to see that Fe^0-BC-1200 showed the best removal ability on RB, with the removal efficiency reaching more than 99% after 30 min, followed by Fe^0-BC-1100, with the removal efficiency of 86%. However, the three other materials exhibited relatively low removal ability, with the removal efficiency was under 60%. Compared with the XRD results in Figure 3, the presence of Fe^0 was the main difference between these materials, demonstrating that the reduction of Fe played a key role in the removal process of RB. In addition, the order of removal efficiency of the three materials without Fe^0 was Fe^0-BC-800 > Fe^0-BC-900 > Fe^0-BC-1000, which was consistent to that of their specific surface areas (shown in Table 3). This result can be ascribed to the fact that smaller specific surface area implies the lower adsorption sites and worse absorption performance.

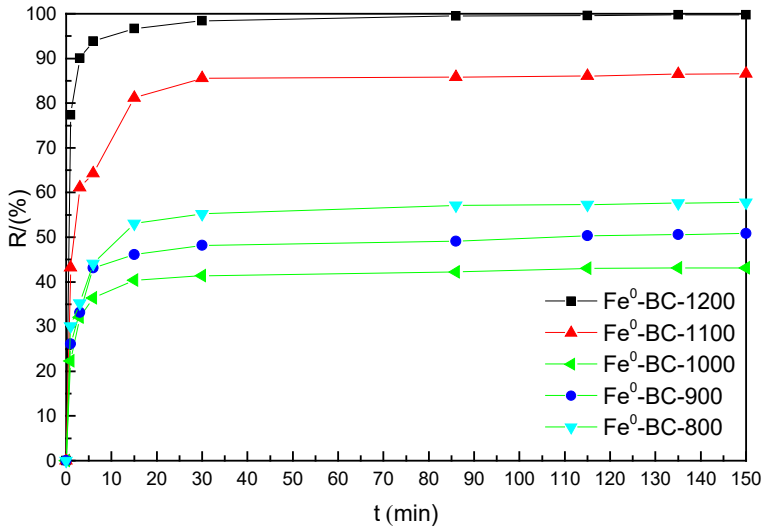

Figure 5. Removal efficiency on RB using various Fe^0-BC materials(C_0=100mg/L, pH=4.02, dosage=2g/L, T=25 ℃).

For in-depth understanding of the effects of Fe^0 and BC on the removal of RB, the removal efficiency of RB on BC-T and Fe^0 powder was investigated. As shown in Figure 6, it is clear that the removal efficiency decreased with the increase of temperature. In general, a high temperature can accelerate carbon graphitization, causing worse adsorption capacity (Yu et al., 2019). Besides, compared the results in Figure 5, the removal efficiency using BC-1000, BC-900 and BC-800 was higher than that of Fe^0-BC-1000, Fe^0-BC-900 and Fe^0-BC-800, respectively. This is because of BC-T contained more biochar at the same dosage, and other compositions in Fe^0-BC-1000, Fe^0-BC-900 and Fe^0-BC-800 had no positive effect on RB removal.Moreover, the ultimate removal efficiency of RB on BC-1200 was only 48%, which was much lower than that of Fe^0-BC-1200, whereas the Fe^0 powder had no removal ability on RB, with the removal efficiency of 0%. The result suggested that the favorable removal efficiency of RB on Fe^0-BC-1200 was attributed to the interaction of various multiple components. As a reducing active site, the presence of Fe^0 on biochar surface could effectively degrade RB, and the removal efficiency improved simultaneously.

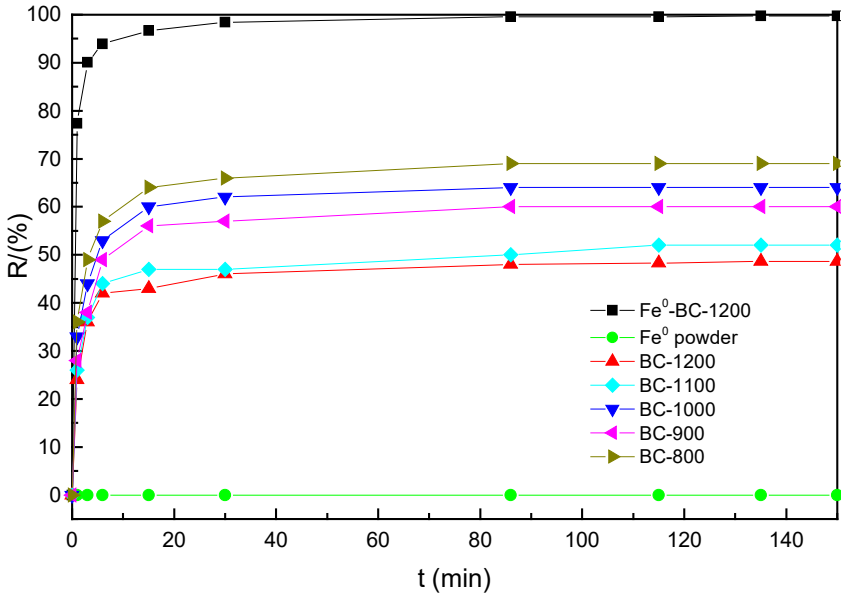

Figure 6. Removal efficiency on RB using BC and Fe^0 powder (C_0=100mg/L, pH=4.02, dosage=2g/L, T=25 ℃).

From the above results, it can be indicated that the main factors affecting removal efficiency of RB on Fe^0-BC were the amount of Fe^0 particles and the specific surface area, while the Fe^0 particles had dominant influence. Consequently, a high temperature is necessary to obtain Fe^0-BC with better performance on RB removal due to more Fe^0 particles generated.

Adsorption kinetic

The removal capacities of RB on Fe^0-BC-1200 and the linear transformed models of the pseudo-first-order and pseudo-second-order models are presented in Figure 7. As shown in Figure 7(a), RB was removed rapidly in the first 10 min and tends to balance after 20 min. The structure of Fe^0-BC-1200 with high specific surface area accelerated the mass transfer process, which is benefit to improve the removal rate of RB. Table 4 shows the fitting kinetics parameters in Figure 7(a) and Figure 7(b). Clearly, the goodness of fit (R^2) of the pseudo-second-order model was 0.9998, which is much higher than that of the pseudo-first-order model of 0.8256. Moreover, the q_e calculated by pseudo-second-order was 49.93 mg/g, that was in good agreement with the experimental data compared with the pseudo-first-order model of 7.46 mg/g. Therefore, the pseudo-second-order model fits well to the experiment data, indicated that the removal process of RB by Fe^0-BC-1200 resulted from the synergetic effect including physical and chemical adsorption.

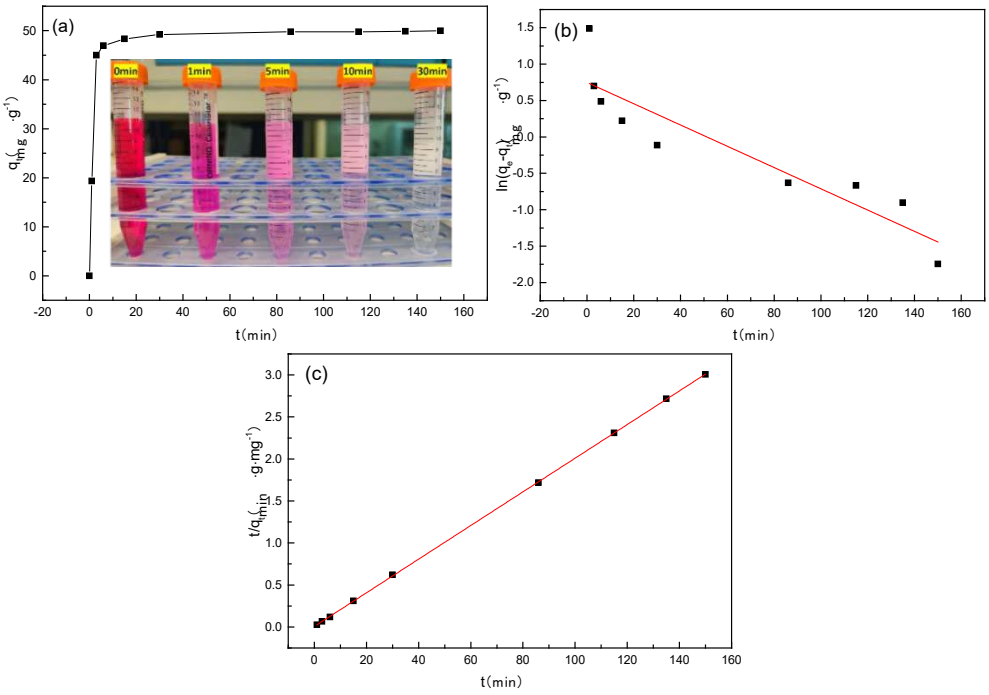

Figure 7. Removal capacities of RB on Fe^0-BC-1200 with time(a), kinetic liner plots of pseudo-first-order model (b) and pseudo-second-order model (c) (C_0=100mg/L, pH=4.02, dosage=2g/L, T=25 ℃).

Table 4 Kinetics parameters for sorption of RB on Fe-C-1200

Pseudo-first-order model			Pseudo-second-order model		
q_e(mg/g)	k_1(min^{-1})	R^2	q_e(mg/g)	k_2(g/(mg·min))	R^2
7.46	0.014	0.8256	49.93	0.0062	0.9998

Effect of pH on RB removal

Usually, rhodamine B wastewater has acidic property. Thus, the effect of various initial pH values on RB removal by Fe^0-BC-1200 was investigated under acidic conditions, and the results are shown in Figure 8. Within 1 min, the removal efficiencies were 99%, 90%, 77%, and 82% at initial pH values of 1.5, 2.5, 4.02, and 6, respectively. This trend showed that the removal rate significantly increased with the decrease of pH. The reasons of this fact are presented as follows: On the one hand, Fe^0 is more easily oxidized to Fe^{2+} under acidic conditions as presented in Eq. (7) (Peng et al., 2017; Li et al., 2017), and the reaction with RB was promoted at the same time; on the other hand, some polar groups were generated on the biochar surface during the adsorption process, and these polar groups displayed the ability of polarized adsorption under acidic conditions (Zhang et al., 2018; Qian et al., 2017).Thus, the adsorption capacity of biochar was enhanced. Moreover, above 99% removal efficiency was obtained within 30 min at all tested initial pH values. It revealed that the prepared Fe^0-BC-1200 could exhibit outstanding removal capacity in practical situation.

$$Fe^0 + H_2O \longrightarrow Fe^{2+} + H_2 + 2OH^- \quad (7)$$

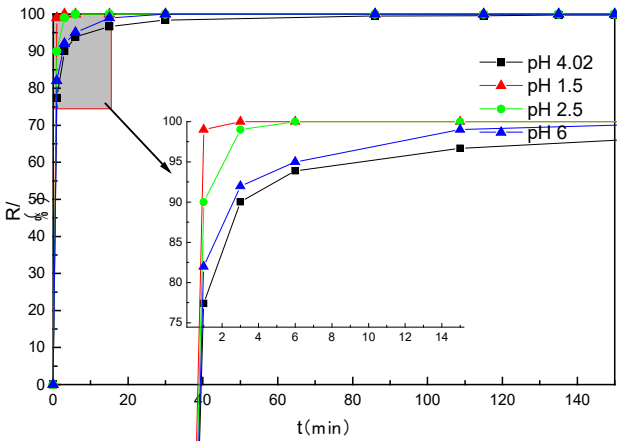

Figure 8. Effects of initial solution pH on removal efficiency by Fe^0-BC-1200 (C_0=100mg/L, dosage=2g/L, T=25 ℃).

In order to futher investigate the effect of pH on the removal of RB, the solution pH values were determined at different selected reaction time, and the results are shown in Figure 9. From the picture, the curves of pH value with time presented the same trend as follows: a rapid increase at first, followed by decrease, and then a slow increase again, and eventually stabilized at about 9. This finding could be explained as follows. The reaction between Fe^0 and H_2O (Eq. (7)) was conducted rapidly when Fe^0-BC-1200 was added to the RB solution. Slight oxidation occurred on the surface and a large amount of H_2 was produced in a short time. Therefore, the pH value increased rapidly at first. Then, due to the severe oxidation or corrosion on the surface of Fe^0 and the accumulation of Fe^{2+} and H_2, the reaction rate of Eq. (7) was less than that of Eq. (8), so Fe^{2+} was reduced and pH value decreased at the same time. At last, the pH value increased again, which may be ascribed to the formation of a coupling pair between Fe^0 and Cu^0. Because of the high standard electrode potentials difference betwwen Fe^0 (-0.44V) and Cu^0 (0.34V) (Bratsch and Steven, 1989), the electrical current flowed from relatively active Fe^0 to Cu^0 and the active atom hydrogen (H^*) was simultaneously generated with H^+ adsorbed on the copper surface (Eq. (9)) (Wang et al., 2017) and the presence of H^* reinforced the reduced process of RB (Xiong et al., 2016). Due to the consumption of H^+, the pH value increased again, and finally reached the equilibrium state. As one of the most important physical and chemical parameters in this reaction system, the change of pH value demonstrated that Cu^0 may play a catalytic role in RB removal by Fe^0-BC-1200.

$$Fe^{2+} + 2e^- \longrightarrow Fe^0 \quad (8)$$

$$FeCu + H^+ + e^- \longrightarrow FeCuH^* \quad (9)$$

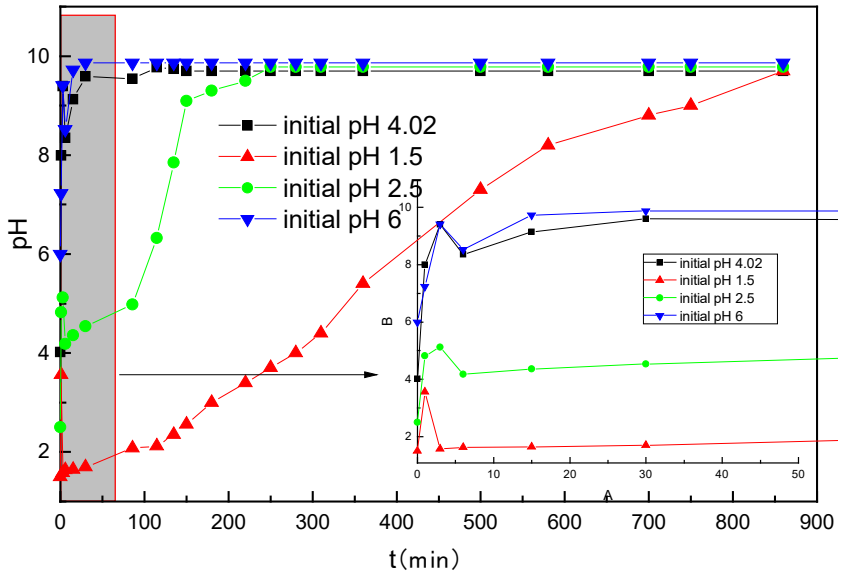

Figure 9. Solution pH at different selected sample time (C_0=100mg/L, dosage=2g/L, T=25 ℃).

Mechanisms analysis

The residual products at different reaction time during the process of RB removal by Fe^0-BC-1200 were detected by LCMC, and the results are shown in Figure 10. Figure 10(a) presents the mass spectra of RB solution without adding Fe^0-BC-1200, m/z 443 and 444 were molecular ion peaks of RB ions or its isotopes. The molecular iron peaks of RB were strong and its molecular fragment peaks were small and weak. Thus, the RB molecular structure was possibly not destroyed under ESI MS. As shown in Figure 10(b), the result of MS at 1 min was basically consistent with that of Figure 10(a), indicating that RB was not degraded in the first 1min. However, compared with the result in Figure 5, the concentration of RB decreased by 77% within 1 min, this finding proved that the l RB removal is mainly reached by physical adsorption in the early stage. As shown in Figure 10(c), new molecular ion peaks were observed in the MS result at 15 min, among which m/z 331 was the molecular ion peak of RB with four ethyl groups removed (Horikoshi et al., 2002), and m/z 107, 143 and 201 were the molecular iron peaks of small molecule products after the benzene rings in RB were opened (Jun et al., 2020).The molecular ion peak of RB disappeared and the molecular iron peak of small molecules strengthened in the result of mass spectrometry at 30min, as shown in Figure 10(d), indicating that RB was completely degraded. The above results confirm that RB was degraded in the removal process.

To further understand the mechanisms of Fe^0-BC-1200 for RB removal, the XRD of Fe^0-BC-1200 before and after RB removal were analyzed, and the results were shown in Figure 11. After reacting with the RB solution, the diffraction peaks of Fe^0 located at 44.2°, 65.0° and 82.3° weakened and the diffraction peaks of Fe_2O_3 and Fe_3O_4 located at 64.1° and 35.4° were detected, illustrating that the redox reaction occurred

between Fe^0 and RB and Fe^0 was oxidized to Fe^{2+} and Fe^{3+}. Therefore, Fe^0-BC-1200 is considered an efficient reductant to remove RB. In addition, the phase of Cu showed no difference, indicating that Cu^0 only play a catalytic role and did not participate directly in the degradation of RB.

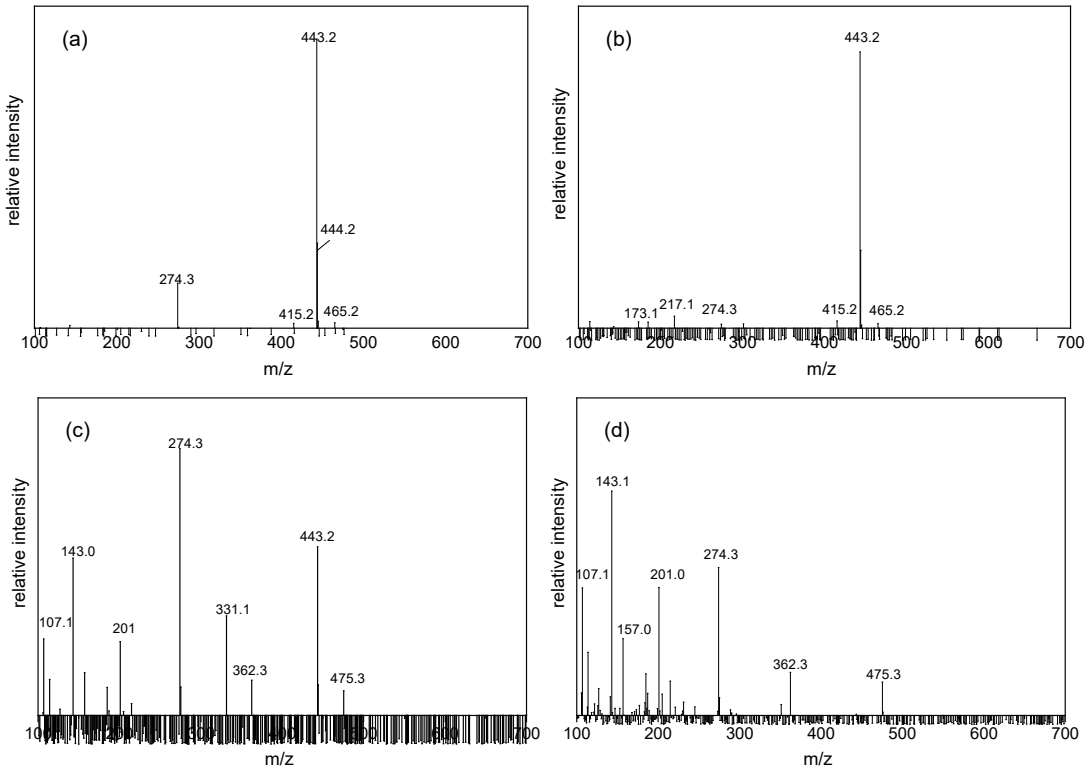

Figure 10. Mass spectra of RB at different reaction time: (a) 0min, (b) 1min, (c) 15min, (d) 30min.

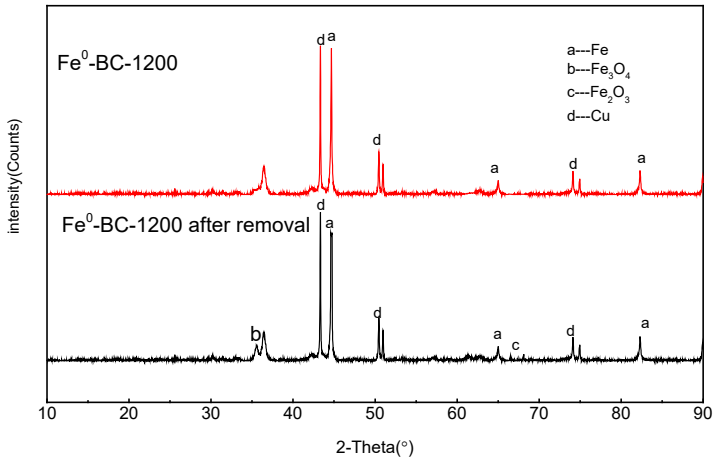

Figure 11. XRD patterns of Fe^0-BC-1200 before and after removal of RB

Based on the above results, it can be concluded that the removal mechanism of Rb by Fe^0-BC-1200 mainly includes the following: 1) In the initial stage of reaction, RB was adsorbed on the surface of biochar mainly through physical adsorption; 2) Subsequently, abundant microscopic primary cells formed between the Fe^0 particles located on the biochar surface and biochar itself. The presence of Cu catalyzed this process, and the electrons flowed to Cu^0 with low potential, thereby promoting the corrosion of Fe^0, accelerating the electron transfer with RB. This redox action destroyed

the C-N bond of the RB molecular branched chain and removed ethyl. Then the deethylated products underwent ring-opening reaction and generated many organic compounds with small mass charge ratio, followed by complete degradation. The mechanism diagram of RB removal by Fe^0-BC-1200 is presented in Figure 12.

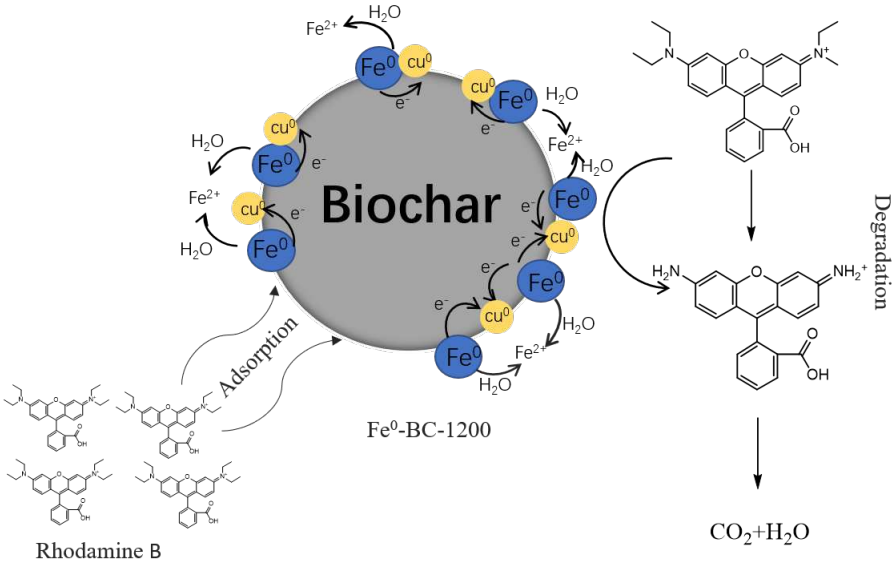

Figure 12. Mechanism diagram of RB removal by Fe^0-BC-1200.

Conclusions

In this study, wood waste and iron sludge were used as carbon and iron sources, respectively, and a new process was proposed to synthesize the zero-valent iron/biochar (Fe^0-BC) by carbothermal reduction under the condition of oxygen isolation. Characterization results showed that Fe^0-BC-1200 prepared at 1200 ℃ has the advantages of large specific surface area, small granularity of Fe^0 particles and high Fe^0 loading on the biochar surface. Besides, Fe^0-BC-1200 showed excellent performance on removal of RB, and the equilibrium adsorption capacity reached 49.93 mg/g when the initial concentration of RB and the dosage of Fe^0-BC-1200 were 100 mg/L and 2g/L, respectively. The pseudo-second-order model was suitable to fit the removal experimental data. Meanwhile, the removal mechanism included the physical adsorption of biochar and the redox reaction of Fe^0. The presence of Cu^0 was conducive to catalyze the oxidation of iron, thus enhancing the degradation effect. Therefore, the carbon supported by the zero-valent iron material prepared by carbothermal reduction process with low cost of raw materials, no additional reductant, simple operation, and significant detoxification effect, has the potential of industrial production.

Declarations

Ethics approval and consent to participate Not applicable

Consent for publication Not applicable

Availability of data and materials The datasets used and analysed during the current study are available from the corresponding author on reasonable request.

Competing Interests The authors declare that they have no conflict of interest.

Authors Contributions Jianguo Liu contributed to the conception of the study; Chao Chen, Chao Gen and Wenzhi Qi performed the experiment; Chao Chen performed the data analyses and wrote the manuscript; Qin Liu, Xuetao Zhu and Fang Wang helped perform the analysis with constructive discussions. All authors commented on previous versions of the manuscript and approved the final manuscript.

Acknowledgements and funding information The authors are grateful for the support of National Key R&D Program of China (Grant No. 2108YFC1902906), the natural science foundation of China (No. 51674018), and the Postdoctoral Sustentation Fund, China (Grant No. 2018M631488).

References

Bakshi, S., Banik, C., Rathke, S. J., Laird, D. A., 2018. Arsenic sorption on zero-valent iron-biochar complexes. Water research, 137, 153-163.

Bratsch, S. G., 1989. Standard electrode potentials and temperature coefficients in water at 298.15 K. Journal of Physical and Chemical Reference Data, 18(1), 1-21.

Barzegar, G., Jorfi, S., Zarezade, V., Khatebasreh, M., Mehdipour, F., Ghanbari, F., 2018. 4-Chlorophenol degradation using ultrasound/peroxymonosulfate/nanoscale zero valent iron: reusability, identification of degradation intermediates and potential application for real wastewater. Chemosphere 201, 370-379.

Calderon B., Fullana A., 2015. Heavy metal release due to aging effect during zero valent iron nanoparticles remediation. Water research, 83, 1-9.

Chen, C., Sun, T., Wang, X., Hu, T., 2017. Effects of MgO on the reduction of vanadium titanomagnetite concentrates with char. JOM, 69(10), 1759-1766.

Chen, C., Sun, T., Geng, C., Kou, J., Liu, J., 2019. Formation and Mechanism of Magnesium Titanate in the Process of Ilmenite Reduction. Mineral Processing and Extractive Metallurgy Review, 1-10.

Chen, X., Chen, G., Chen, L., Chen, Y., Lehmann, J., McBride, M.B., Hay, A.G., 2011.Adsorption of copper and zinc by biochars produced from pyrolysis of hardwood andcorn straw in aqueous solution. Bioresource technology, 102(19), 8877-8884.

Demirbaş, A., 2005. Estimating of structural composition of wood and non-wood biomass samples. Energy Sources, 27(8), 761-767.

Devi, P., Saroha, A. K., 2014. Synthesis of the magnetic biochar composites for use as an adsorbent for the removal of pentachlorophenol from the effluent. Bioresource

Technology, 169, 525-531.
Dewage, N. B., Liyanage, A. S., Pittman Jr, C. U., Mohan, D., Mlsna, T., 2018. Fast nitrate and fluoride adsorption and magnetic separation from water on α-Fe_2O_3 and Fe_3O_4 dispersed on Douglas fir biochar. Bioresource technology, 263, 258-265.
Dong, H., Zhang, C., Hou, K., Cheng, Y., Deng, J., Jiang, Z., Tang., Zeng, G., 2017. Removal of trichloroethylene by biochar supported nanoscale zero-valent iron in aqueous solution. Separation and Purification Technology, 188, 188-196.
Dong, W., Lee, C. W., Lu, X., Sun, Y., Hua, W., Zhuang, G., Zhao, D., 2010. Synchronous role of coupled adsorption and photocatalytic oxidation on ordered mesoporous anatase TiO_2-SiO_2 nanocomposites generating excellent degradation activity of RhB dye. Applied Catalysis B: Environmental, 95 (3-4), 197-207.
Du, Q., Zhang, S., Song, J., Zhao, Y., Yang, F., 2020. Activation of porous magnetized biochar by artificial humic acid for effective removal of lead ions. Journal of Hazardous Materials, 389, 122115.
Emandi, A., Vasiliu, C. I., Budrugeac, P., Stamatin, I., 2011. Quantitative investigation of wood composition by integrated ft-ir and thermogravimetric methods. Cellulose Chemistry and Technology, 45(9), 579-584.
Frick, H., Tardif, S., Kandeler, E., Holm, P., Brandt, K., 2018. Assessment of biochar and zero-valent iron for in-situ remediation of chromated copper arsenate contaminated soil. Science of the Total Environment, 655, 414-422.
Geng, C., Chen, C., Shi, X., Wu, S., Jia, Y., Du, B., Liu, J. 2020. Recovery of metals from municipal solid waste incineration fly ash and red mud via a co-reduction process. Resources, Conservation and Recycling, 154, 104600.
Geng, C., Liu, J., Wu, S., Jia, Y., Du, B., Yu, S., 2020. Novel method for comprehensive utilization of MSWI fly ash through co-reduction with red mud to prepare crude alloy and cleaned slag. Journal of hazardous materials, 384, 121315.
Ghariani, B., Messaoud, M., Louati, I., Mtibaà, R., Nasri, M., Mechichi, T., 2019. Removal of Acid Orange 51 by micro zero-valent iron under different operational conditions and evaluation of toxicity. Environmental Science and Pollution Research, 26(18), 18392-18402.
Han, B., Song, L., Li, H., Song, H., 2019. Naked oats biochar-supported nanoscale zero-valent iron composite: effects on Cd immobilization and enzyme activities in Ulansuhai River sediments of China. Journal of Soils and Sediments, 19(5), 2650-2662.
Hoch, L.B., Mack, E.J., Hydutsky, B.W., Hershman, J.M., Skluzacek, J.M., Mallouk, T.E., 2008. Carbothermal synthesis of carbon-supported nanoscale zero-valent iron particles for the remediation of hexavalent chromium. Environmental science & technology, 42(7), 2600-2605.
Horikoshi, S., Hidaka, H., & Serpone, N., 2002. Environmental remediation by an integrated microwave/UV-illumination method. 1. Microwave-assisted degradation of rhodamine-B dye in aqueous TiO_2 dispersions. Environmental science & technology, 36(6), 1357-1366.
Huang, H., Yao, W., Li, R., Ali, A., Du, J., Guo, D., Xiao, R., Guo, Z., Zhang, Z.,

Awasthi, M. K., 2018. Effect of pyrolysis temperature on chemical form, behavior and environmental risk of Zn, Pb and Cd in biochar produced from phytoremediation residue. Bioresource technology, 249, 487-493.

Huang, H., Zhang, J., Jiang, L., Zang, Z., 2017. Preparation of cubic Cu_2O nanoparticles wrapped by reduced graphene oxide for the efficient removal of rhodamine B. Journal of Alloys and Compounds, 718, 112-115.

Hussain, I., Li, M., Zhang, Y., Li, Y., Huang, S., Du, X., Liu, G., Hayat, W., Anwar, N., 2017. Insights into the mechanism of persulfate activation with nZVI/BC nanocomposite for the degradation of nonylphenol. Chemical Engineering Journal, 311, 163-172.

Jun, B. M., Elanchezhiyan, S. S., Yoon, Y., Wang, D., Kim, S., Prabhu, S. M., Park, C. M., 2020. Accelerated photocatalytic degradation of rhodamine B over carbonate-rich lanthanum-substituted zinc spinel ferrite assembled reduced graphene oxide by ultraviolet (UV)-activated persulfate. Chemical Engineering Journal, 124733.

Kong, L., Zhang, H., Shih, K., Su, M., Diao, Z., Long, J., Chen, D., 2018. Synthesis of FC-supported Fe through a carbothermal process for immobilizing uranium. Journal of hazardous materials, 357, 168-174.

Lawrinenko, M., Wang, Z., Horton, R., Mendivelso-Perez, D., Smith, E. A., Webster, T. E., van Leeuwen, J. H., 2017. Macroporous carbon supported zerovalent iron for remediation of trichloroethylene. ACS Sustainable Chemistry & Engineering, 5(2), 1586-1593.

Li, H., Zhu, F., He, S., 2019. The degradation of decabromodiphenyl ether in the e-waste site by biochar supported nanoscale zero-valent iron/persulfate. Ecotoxicology and environmental safety, 183, 109540.

Li, X., Zhao, Y., Xi, B., Meng, X., Gong, B., Li, R., Liu, H., 2017. Decolorization of methyl orange by a new clay-supported nanoscale zero-valent iron: synergetic effect, efficiency optimization and mechanism. Journal of Environmental Sciences, 52, 8-17.

Li, Z., Sun, Y., Yang, Y., Han, Y., Wang, T., Chen, J., Tsang, D. C., 2020. Biochar-supported nanoscale zero-valent iron as an efficient catalyst for organic degradation in groundwater. Journal of hazardous materials, 383, 121240.

Liu, F., Zuo, J., Chi, T., Wang, P., Yang, B., 2015. Removing phosphorus from aqueous solutions by using iron-modified corn straw biochar. Frontiers of Environmental Science & Engineering, 9(6), 1066-1075.

Liu, H., Chen, T., Xie, Q., Zou, X., Chen, C., Frost, R. L., 2015. The functionalization of limonite to prepare NZVI and its application in decomposition of p-nitrophenol. Journal of Nanoparticle Research, 17(9), 374.

Liu, J., Yu, Y., Zhu, S., Yang, J., Song, J., Fan, W., Yu, H., Bian, D., Huo, M., 2018. Synthesis and characterization of a magnetic adsorbent from negatively-valued iron mud for methylene blue adsorption. PloS one, 13(2), e0191229.

Liu, W., Chen, X., Li, W., Yu, Y., Yan, K., 2014. Environmental assessment, management and utilization of red mud in China. Journal of Cleaner Production, 84, 606-610.

Lops, C., Ancona, A., Di Cesare, K., Dumontel, B., Garino, N., Canavese, G., Hérnandez, S., Cauda, V., 2019. Sonophotocatalytic degradation mechanisms of Rhodamine B dye via radicals generation by micro-and nano-particles of ZnO. Applied Catalysis B: Environmental, 243, 629-640.

Mandal, S., Sarkar, B., Bolan, N., Ok, Y. S., Naidu, R., 2017. Enhancement of chromate reduction in soils by surface modified biochar. Journal of environmental management, 186, 277-284.

Mitzia, A., Vítková, M., Komárek, M., 2020. Assessment of biochar and/or nano zero-valent iron for the stabilisation of Zn, Pb and Cd: A temporal study of solid phase geochemistry under changing soil conditions. Chemosphere, 242, 125248.

Oh, S.Y., Seo, Y.D., Ryu, K.S., 2016. Reductive removal of 2, 4-dinitrotoluene and 2, 4-dichlorophenol with zero-valent iron-included biochar. Bioresource technology, 2016, 216, 1014-1021.

Oleszczuk, P., Kołtowski, M., 2017. Effect of co-application of nano-zero valent iron and biochar on the total and freely dissolved polycyclic aromatic hydrocarbons removal and toxicity of contaminated soils. Chemosphere, 2017, 168, 1467-1476.

Pani, B., Chandrasekhar, P., Singh, S., 2019. Investigation of erosion behaviour of an iron-mud filled glass-fibre epoxy hybrid composite. Bulletin of Materials Science, 42(5), 217.

Peng, A., Huang, M., Chen, Z., Gu, C., 2017. Oxidative coupling of acetaminophen mediated by Fe^{3+}-saturated montmorillonite. Science of The Total Environment, 595, 673-680.

Pourrezaei, P., Alpatova, A., Khosravi, K., Drzewicz, P., Chen, Y., Chelme-Ayala, P., ElDin, M.G., 2014. Removal of organic compounds and trace metals from oil sands process-affected water using zero valent iron enhanced by petroleum coke. Journal of environmental management. 139, 50-58.

Qian, J., Shen, M., Wang, P., Wang, C., Li, K., Liu, J., Lu, B., Tian, X., 2017. Perfluorooctane sulfonate adsorption on powder activated carbon: effect of phosphate (P) competition, pH, and temperature. Chemosphere, 182, 215-222.

Qin, Y., Long, M., Tan, B., Zhou, B., 2014. RhB adsorption performance of magnetic adsorbent Fe3O4/rGO composite and its regeneration through a Fenton-like reaction. Nano-Micro Letters, 6(2), 125-135.

Reddy, A.V.B., Yusop, Z., Jaafar, J., Reddy, Y.V.M., Bin Aris, A., Majid, Z.A., Talib, J., Madhavi, G., 2016. Recent progress on Fe-based nanoparticles: synthesis, properties, characterization and environmental applications. Journal of environmental chemical engineering, 4(3), 3537-3553.

Shang, J., Zong, M., Yu, Y., Kong, X., Du, Q., Liao, Q., 2017. Removal of chromium (VI) from water using nanoscale zerovalent iron particles supported on herb-residue biochar. Journal of environmental management, 197, 331-337.

Shen, Y., LI, T., Zhang, W., Gao, S., Cui, B., Wei, D., NO_2 Sensing properties of α-Fe2O3 nanoparticles synthesized from pyrite. The Journal of the University of Guizhou (Natural Science), 2019,36(2):1-6.

Sun, Y., Iris, K. M., Tsang, D. C., Cao, X., Lin, D., Wang, L., Feng, Y., 2019. Multifunctional iron-biochar composites for the removal of potentially toxic elements, inherent cations, and hetero-chloride from hydraulic fracturing wastewater. Environment international, 124, 521-532.

Tsoumis, G., 2013. Wood as raw material: source, structure, chemical composition, growth, degradation and identification. Elsevier.

Xiong, Z., Lai, B., Yuan, Y., Cao, J., Yang, P., Zhou, Y., 2016. Degradation of p-nitrophenol (PNP) in aqueous solution by a micro-size Fe^0/O3 process (mFe^0/O3): Optimization, kinetic, performance and mechanism. Chemical Engineering Journal, 302, 137-145.

Wang, L., Yu, K., Li, J. S., Tsang, D. C., Poon, C. S., Yoo, J. C., Baek, K., Ding, S., Hou, D., Dai, J. G., 2018. Low-carbon and low-alkalinity stabilization/solidification of high-Pb contaminated soil. Chemical Engineering Journal, 351, 418-427.

Wang, T., Qin, Y., Cao, Y., Han, B., Ren, J., 2017. Simultaneous addition of zero-valent iron and activated carbon on enhanced mesophilic anaerobic digestion of waste-activated sludge. Environmental Science and Pollution Research, 24(28), 22371-22381.

Yu, W., Sun, Y., Lei, M., Chen, S., Qiu, T., Tang, Q., 2019. Preparation of micro-electrolysis material from flotation waste of copper slag and its application for degradation of organic contaminants in water. Journal of hazardous materials, 361, 221-227.

Zhang, K., Sun, P., Zhang, Y., 2019. Decontamination of Cr (VI) facilitated formation of persistent free radicals on rice husk derived biochar. Frontiers of Environmental Science & Engineering, 13(2), 22.

Zhang, Y., Zuo, S., Zhou, M., Liang, L., Ren, G., 2018. Removal of tetracycline by coupling of flow-through electro-Fenton and in-situ regenerative active carbon felt adsorption. Chemical Engineering Journal, 335, 685-692.

Zhao, L., Zhao, Y., Nan, H., Yang, F., Qiu, H., Xu, X., Cao, X., 2020. Suppressed formation of polycyclic aromatic hydrocarbons (PAHs) during pyrolytic production of Fe-enriched composite biochar. Journal of hazardous materials, 382, 121033.

Zhu, S., Dong, G., Yu, Y., Yang, J., Yang, W., Fan, W., Zhou, D., Liu, J., Zhang, L., Huo, M., Wang, Y., 2018. Hydrothermal synthesis of a magnetic adsorbent from wasted iron mud for effective removal of heavy metals from smelting wastewater. Environmental Science and Pollution Research, 25(23), 22710-22724.

Figures

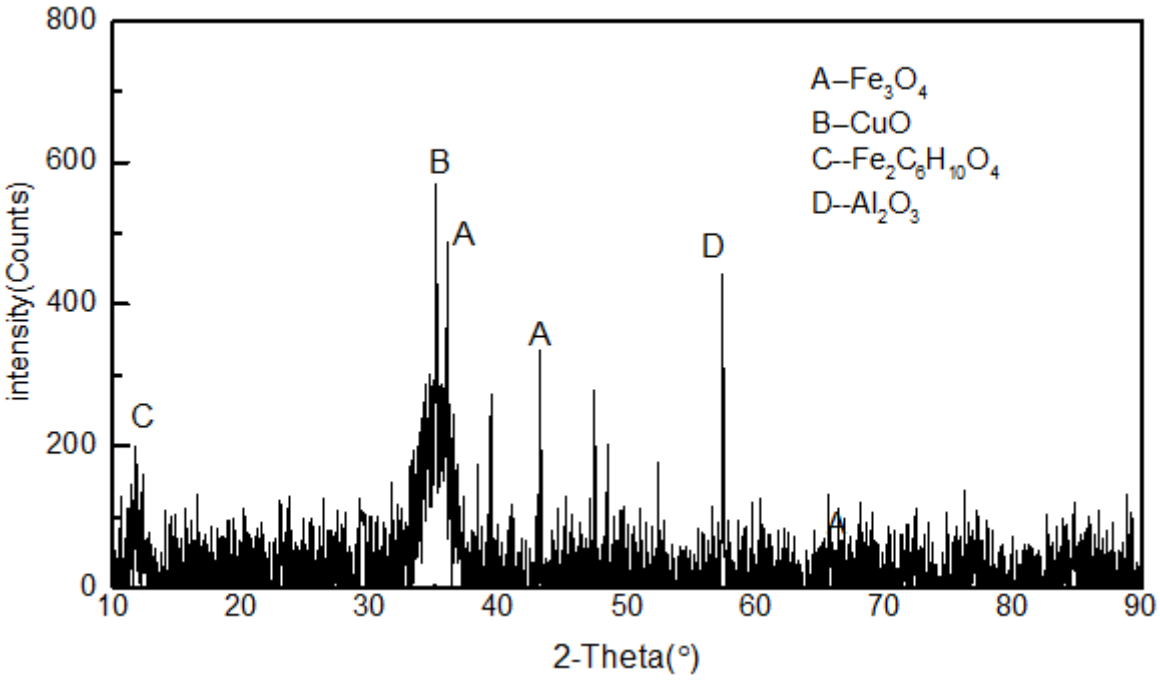

Figure 1

XRD patterns of the iron mud

Figure 2

The preparation process of Fe0-BC

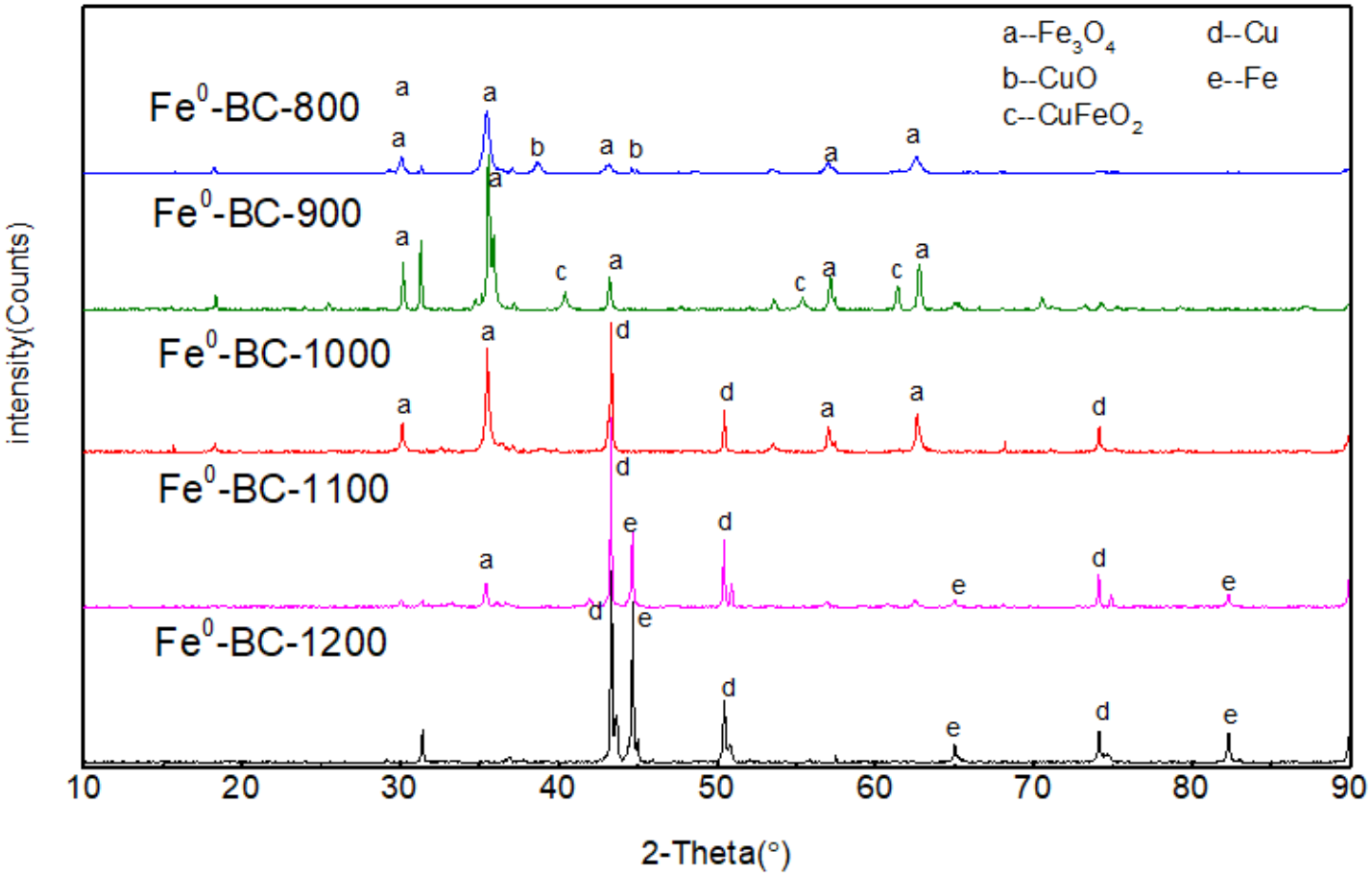

Figure 3

XRD patterns of Fe0-BC

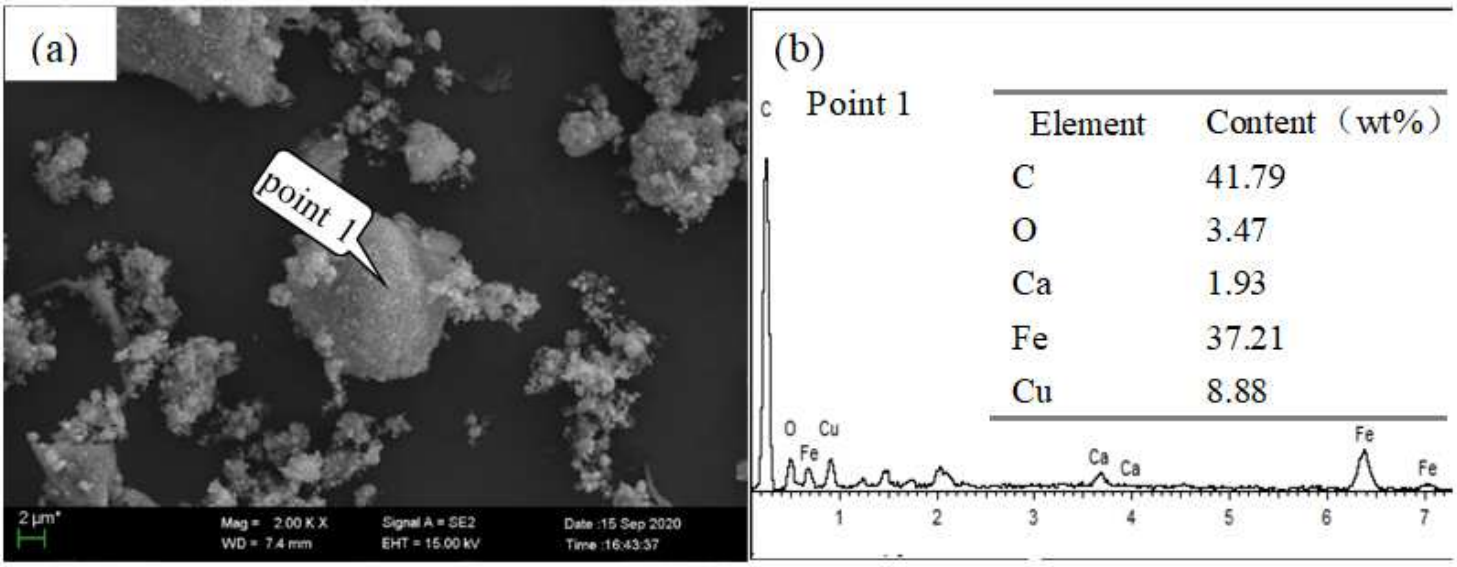

Element	Content（wt%）
C	41.79
O	3.47
Ca	1.93
Fe	37.21
Cu	8.88

Figure 4

SEM image and EDS results of Fe0-BC-1200

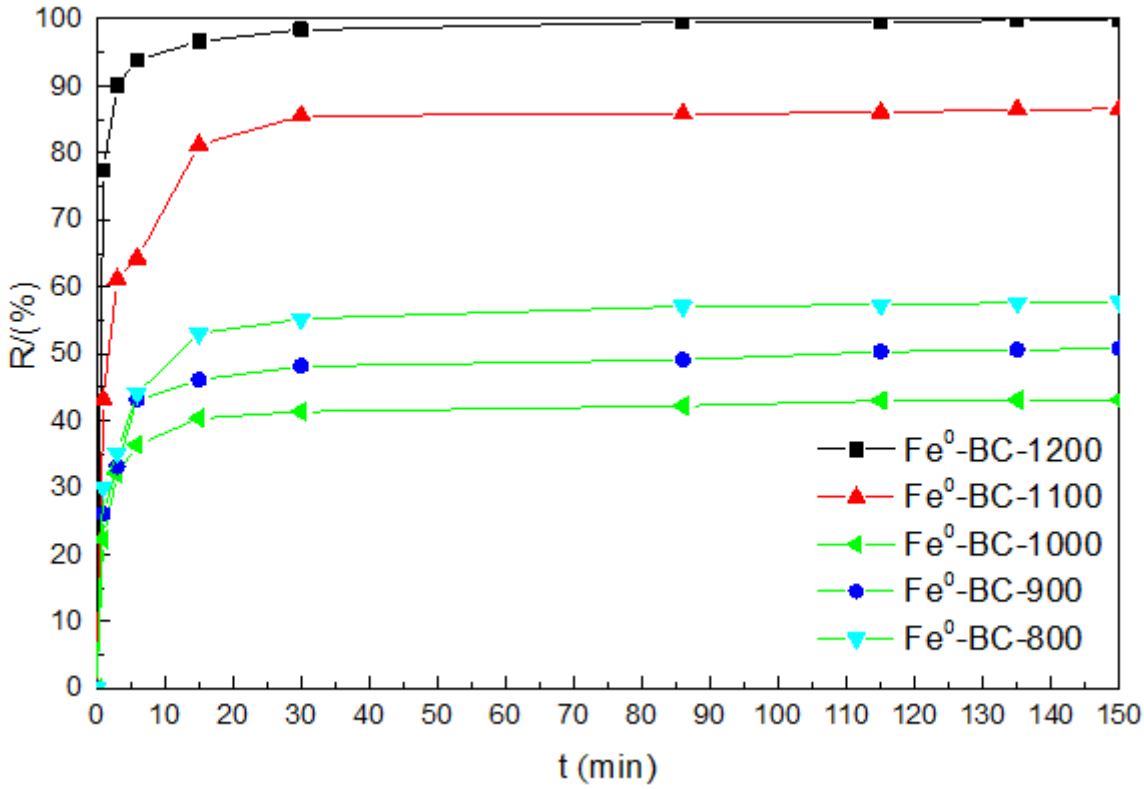

Figure 5

Removal efficiency on RB using various Fe0-BC materials(C_0=100mg/L, pH=4.02, dosage=2g/L, T=25 ℃).

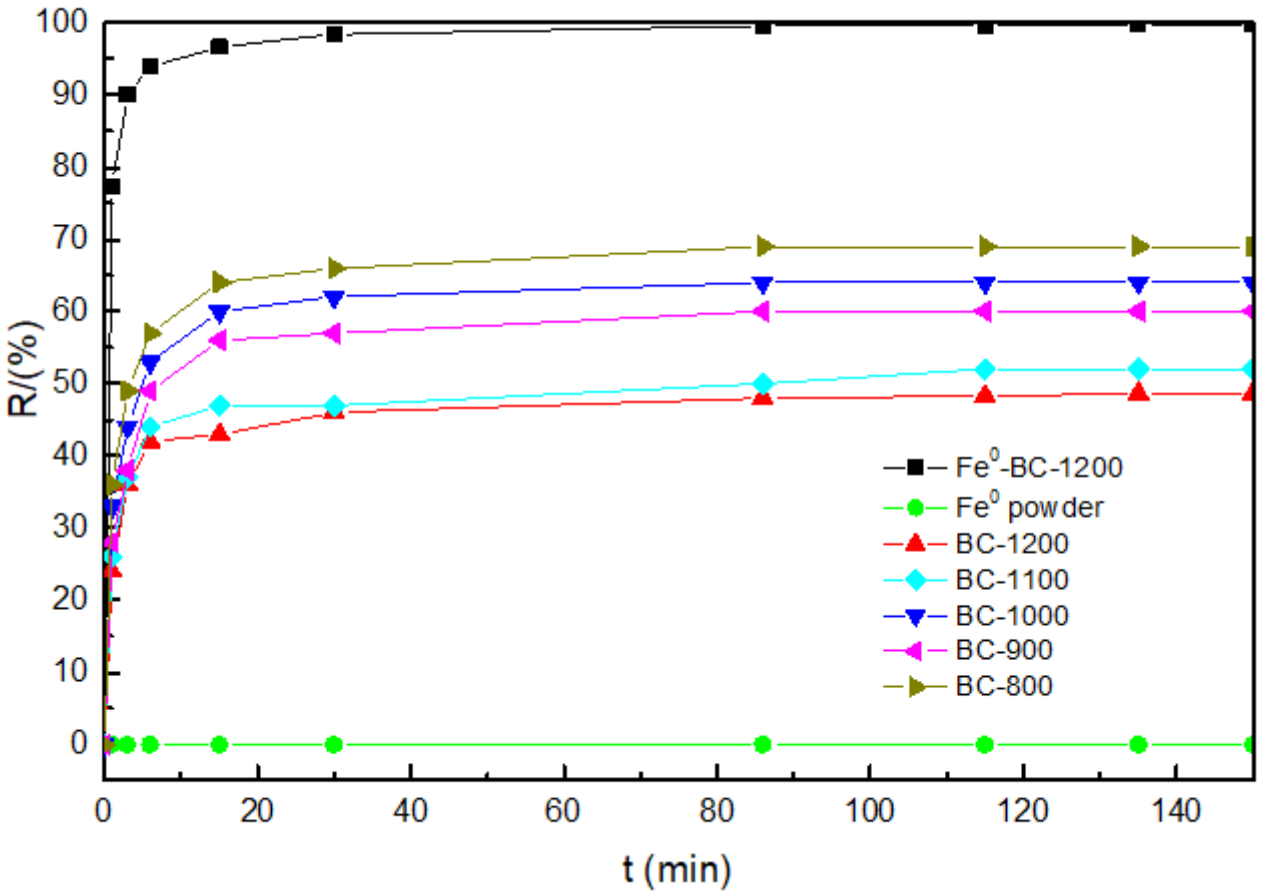

Figure 6

Removal efficiency on RB using BC and Fe0 powder (C_0=100mg/L, pH=4.02, dosage=2g/L, T=25 ℃).

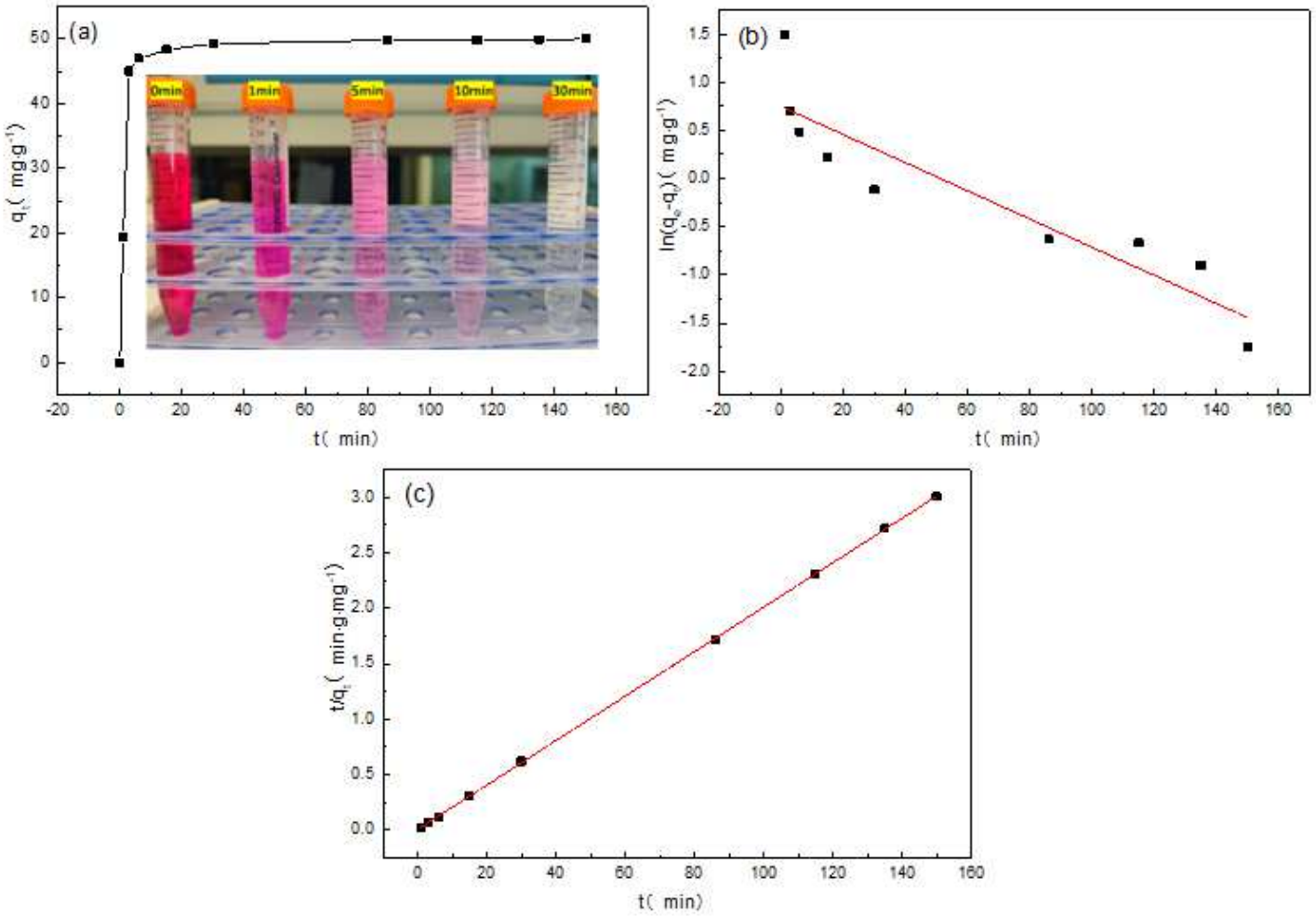

Figure 7

Removal capacities of RB on Fe0-BC-1200 with time(a), kinetic liner plots of pseudo-first-order model (b) and pseudo-second-order model (c) (C_0=100mg/L, pH=4.02, dosage=2g/L, T=25 ℃).

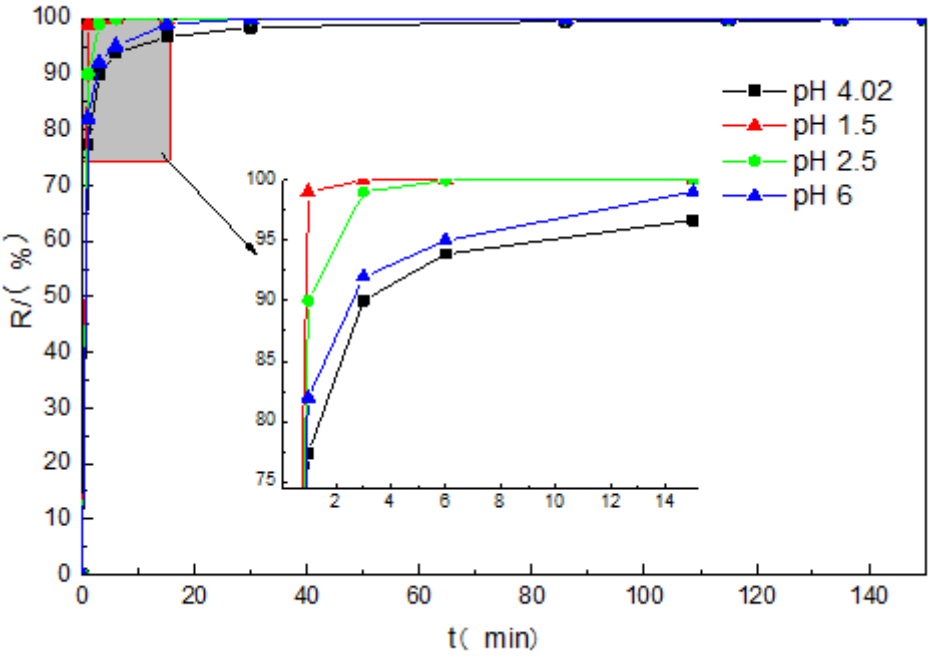

Figure 8

Effects of initial solution pH on removal efficiency by Fe0-BC-1200 (C_0=100mg/L, dosage=2g/L, T=25 ℃).

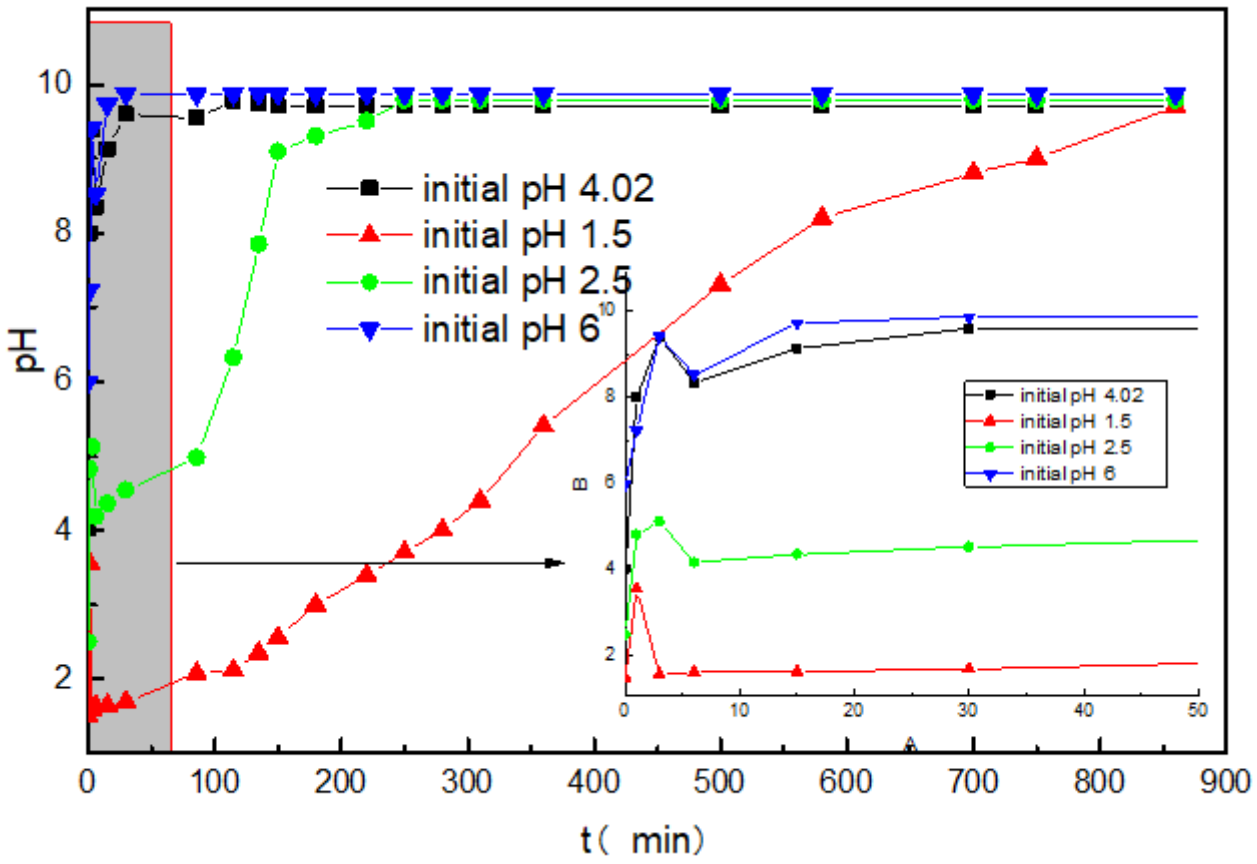

Figure 9

Solution pH at different selected sample time (C_0=100mg/L, dosage=2g/L, T=25 ℃).

Figure 10

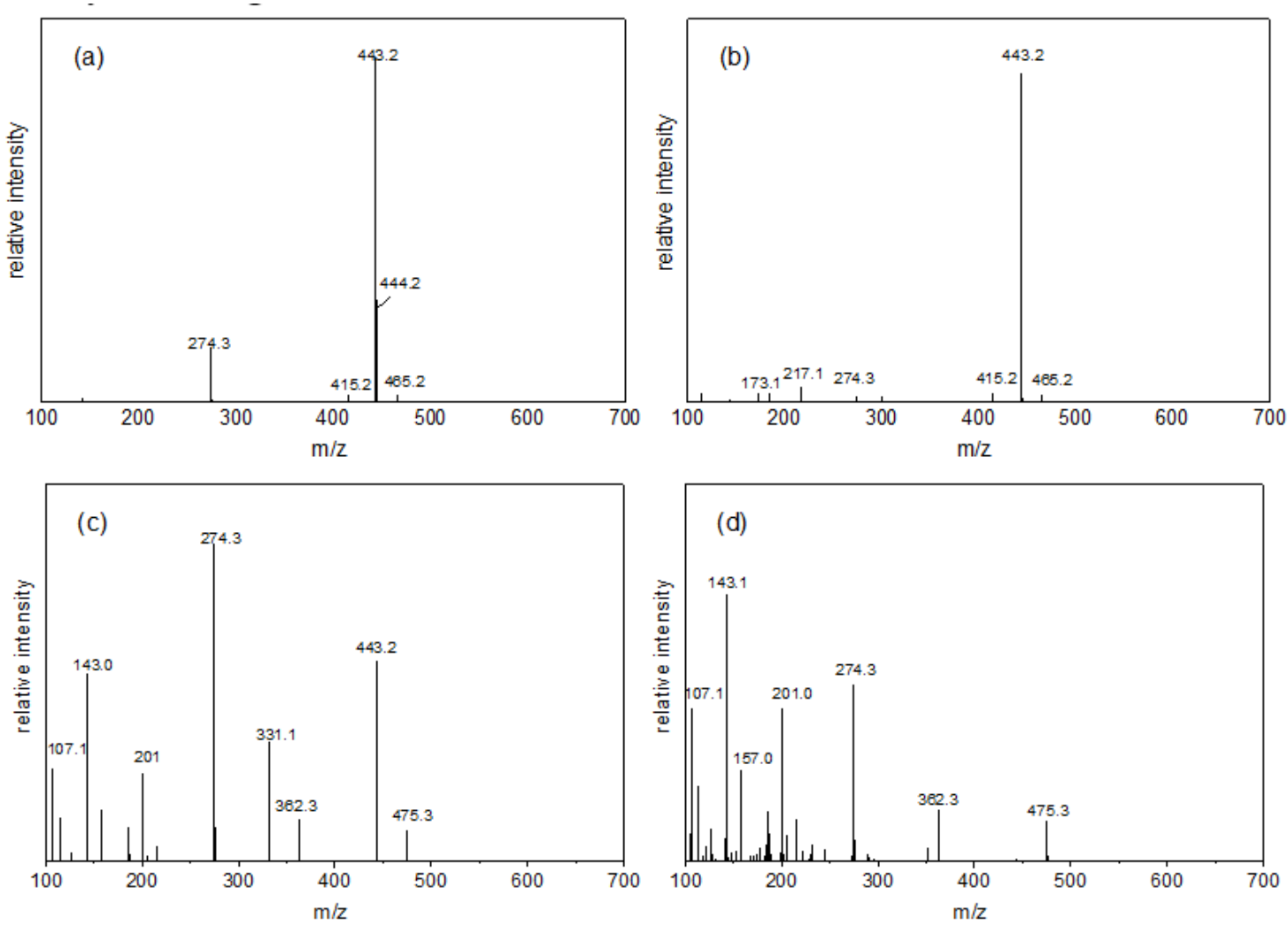

Mass spectra of RB at different reaction time: (a) 0min, (b) 1min, (c) 15min, (d) 30min.

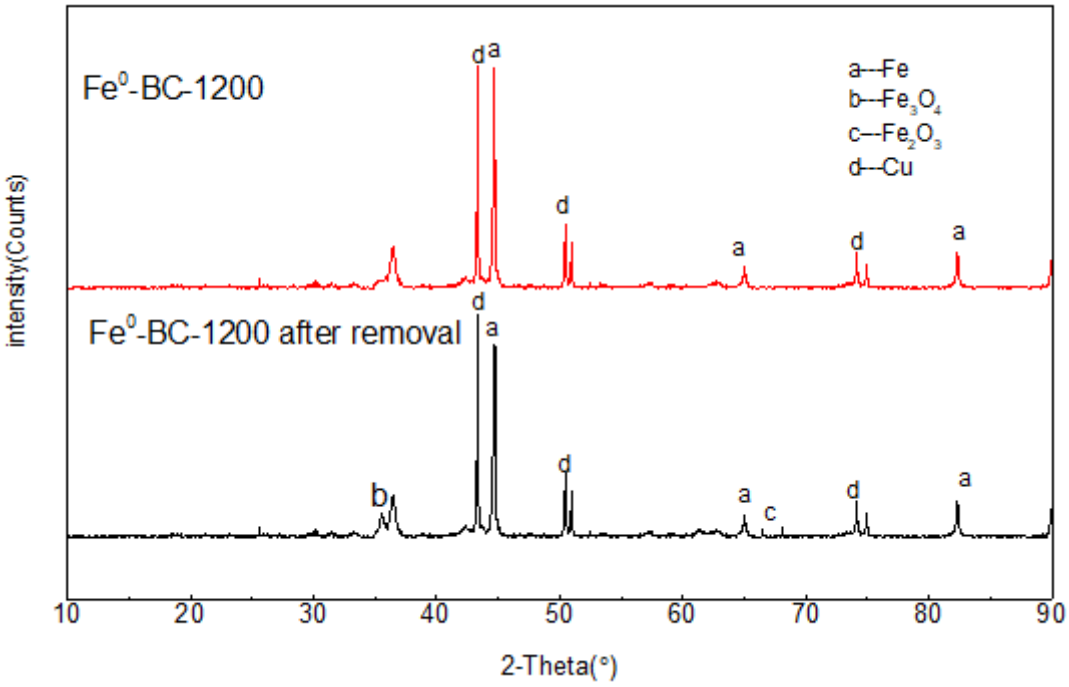

Figure 11

XRD patterns of Fe0-BC-1200 before and after removal of RB

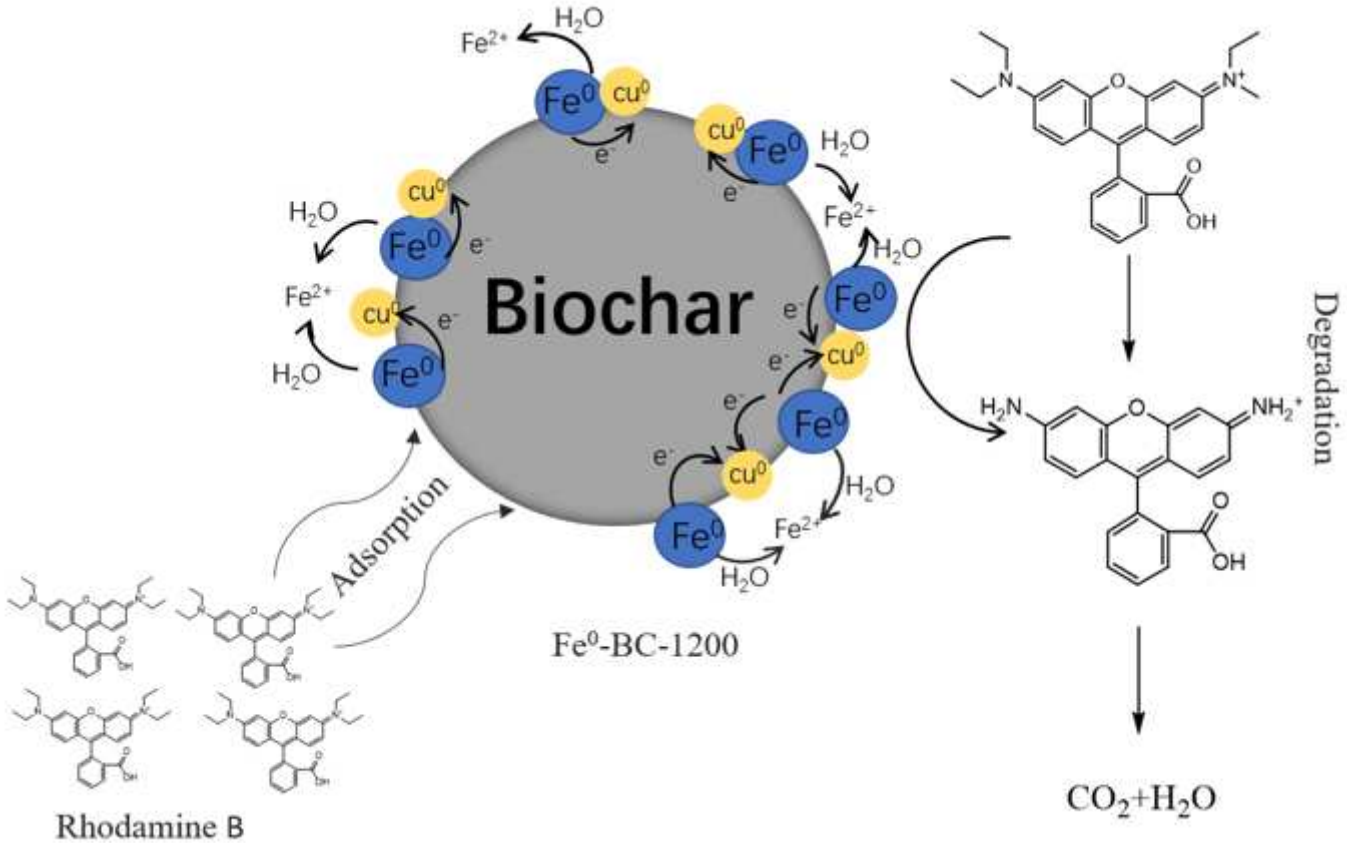

Figure 12

Mechanism diagram of RB removal by Fe0-BC-1200.